



Published in final edited form as:

*Neuroimage*. 2022 April 15; 250: 118962. doi:10.1016/j.neuroimage.2022.118962.

## Differentiation of speech-induced artifacts from physiological high gamma activity in intracranial recordings

Alan Bush<sup>a,b,\*</sup>, Anna Chrabaszcz<sup>c</sup>, Victoria Peterson<sup>a,b</sup>, Varun Saravanan<sup>a,d</sup>, Christina Dastolfo-Hromack<sup>e,g</sup>, Witold J. Lipski<sup>f</sup>, R. Mark Richardson<sup>a,b</sup>

<sup>a</sup>Brain Modulation Lab, Department of Neurosurgery, Massachusetts General Hospital, 225 Charles St, 02114 Thier Research Building, Suite 429, Boston, MA 02114, USA

<sup>b</sup>Harvard Medical School, Boston, MA 02115, USA

<sup>c</sup>Department of Psychology, University of Pittsburgh, Pittsburgh, PA 15260, USA

<sup>d</sup>Department of Brain and Cognitive Sciences, Massachusetts Institute of Technology, Cambridge, MA 02139, USA

<sup>e</sup>Department of Communication Science and Disorders, University of Pittsburgh, Pittsburgh, PA 15260, USA

<sup>f</sup>Department of Neurological Surgery, University of Pittsburgh, Pittsburgh, PA 15260, USA

<sup>g</sup>West Virginia University, Communication Science and Disorders, WV 26506, USA

### Abstract

There is great interest in identifying the neurophysiological underpinnings of speech production. Deep brain stimulation (DBS) surgery is unique in that it allows intracranial recordings from both cortical and subcortical regions in patients who are awake and speaking. The quality of these recordings, however, may be affected to various degrees by mechanical forces resulting from speech itself. Here we describe the presence of speech-induced artifacts in local-field potential (LFP) recordings obtained from mapping electrodes, DBS leads, and cortical electrodes. In addition to expected physiological increases in high gamma (60–200 Hz) activity during speech production, time-frequency analysis in many channels revealed a narrowband gamma component that exhibited a pattern similar to that observed in the speech audio spectrogram. This component was present to different degrees in multiple types of neural recordings. We show that this component tracks the fundamental frequency of the participant's voice, correlates with the power spectrum of speech and has coherence with the produced speech audio. A vibration sensor attached to the stereotactic frame recorded speech-induced vibrations with the same pattern

This is an open access article under the CC BY-NC-ND license (<http://creativecommons.org/licenses/by-nc-nd/4.0/>)

\*Corresponding author at: Brain Modulation Lab, Department of Neurosurgery, Massachusetts General Hospital, 225 Charles St, 02114 Thier Research Building, Suite 429, Boston, MA 02114, USA. alan.bush@mgh.harvard.edu (A. Bush).

Author contributions

W.J.L. and R.M.R. designed the experiment and performed the recordings. A.B., A.C., C.D.-H. and W.J.L. reconstructed the electrode localizations and preprocessed the electrophysiological data. A.C. and C.D.-H. overviewed the phonetic coding. A.B., A.C., V.P., V.S., C.D.-H. analyzed data. A.B., A.C. and R.M.R. wrote the manuscript. All authors discussed the results and implications and commented on the manuscript at all stages. The authors declare no competing financial interests.

Supplementary materials

Supplementary material associated with this article can be found, in the online version, at doi:10.1016/j.neuroimage.2022.118962.

observed in the LFPs. No corresponding component was identified in any neural channel during the listening epoch of a syllable repetition task. These observations demonstrate how speech-induced vibrations can create artifacts in the primary frequency band of interest. Identifying and accounting for these artifacts is crucial for establishing the validity and reproducibility of speech-related data obtained from intracranial recordings during DBS surgery.

## Keywords

Intracranial recordings; Deep brain stimulation; Electrocorticography; Local field potentials; Intraoperative research; Speech; High gamma; Artifact

---

## 1. Introduction

Invasive brain recordings performed in awake patients undergoing clinically indicated neurosurgeries provide a unique opportunity to study speech production with better spatial and temporal precision than noninvasive neuroimaging methods. One of the advantages of intracranial recordings is a much higher signal-to-noise ratio (SNR) and larger measurable frequency range. This allows examination of frequency bands above 70 Hz that are typically unattainable with noninvasive methods due to volume conduction effects and a sharp attenuation in power at higher frequencies when passing the skull (Mukamel and Fried, 2012). Many assume that a higher SNR in the intracranial recordings makes them less susceptible to artifacts frequently observed in non-invasive recordings, such as electro-myographic artifacts due to eye, jaw, lip and tongue movement (Flinker et al., 2018; Lachaux et al., 2003; Llorens et al., 2011). Comprehensive quantitative examination of the quality of the signal and identification of potential sources of artifacts in intracranial recordings, however, have received very little attention. Several types of artifacts found in scalp EEG have been described in intracranial recordings, such as eye movement artifacts in fronto-anterior regions (Ball et al., 2009), and facial and mouth movement artifacts in electrodes close to temporal muscles (Otsubo et al., 2008). This suggests that movement artifacts can contaminate intracranial LFP recordings acquired to study the neural control of speech production.

Neural activity in the high gamma frequency band (60–200 Hz) tracks specific features of speech perception and production. For example, increased power in the high gamma frequency range has been observed in the superior temporal gyrus in response to auditory stimuli (Crone et al., 2001; Hamilton et al., 2018; Mesgarani et al., 2014), and in Broca's and motor cortices during speech production (Edwards et al., 2010; Flinker et al., 2015; Mugler et al., 2018). High gamma activity recorded from the Rolandic cortex (pre and postcentral gyri) has been shown to track articulatory and/or acoustic features of speech sounds (Bouchard et al., 2013; Cheung et al., 2016; Chrabaszcz et al., 2019; Conant et al., 2018). Some recent advances have even made it possible to reconstruct speech from the brain's activity in the high gamma band (Anumanchipalli et al., 2019; Martin et al., 2019; Moses et al 2021), pointing at its potential utility for brain-computer interfaces to develop speech prostheses. Contamination of the neural signal with audio acoustics therefore is a potential barrier to decoding the true electrophysiological correlates of speech production.

Given the impact that speech dysfunction can have in patients with movement disorders, and the fact that the role of subcortical regions in speech production are not well understood, we recently developed a strategy to simultaneously record from the cortex and the subcortical implantation target during DBS surgery. With the patient's consent, it is possible to temporarily place an electrocorticography (ECoG) electrode strip on the surface of the brain, a technique that has been used safely in over 500 patients (Panov et al., 2017; Sisterson et al., 2021). Here, we report the systematic identification and quantification of speech-induced artifacts in several types of intracranial electrophysiological recordings obtained using a speech production task performed during DBS implantation surgery. We show that this artifact is caused by mechanical vibrations induced by the produced speech, and that it can also be found in a 'blank' headstage pin not connected to any electrode. The results presented in this study encourage careful assessment of possible audio-induced artifacts in intracranial recordings obtained during speech production research. Additionally, we provide suggestions for data collection and analysis that may reduce the potential for false discoveries.

## 2. Materials and methods

### 2.1. Participants

Participants were English-speaking patients with Parkinson's disease (21 M/8F, age:  $65.6 \pm 7.1$  years, duration of disease:  $6.1 \pm 4.1$  years) undergoing awake stereotactic neurosurgery for implantation of DBS electrodes in the subthalamic nucleus (STN). Dopaminergic medication was withdrawn the night before surgery. All procedures were approved by the University of Pittsburgh Institutional Review Board (IRB Protocol #PRO13110420). All patients provided informed consent to participate in the study.

### 2.2. Behavioral task

Participants performed a syllable triplet repetition task intraoperatively, repeating aloud sequences of CV syllables presented auditorily through earphones. Triplets were presented at either low ( $\sim 50$  dB SPL) or high ( $\sim 70$  dB SPL) volume and participants were instructed to produce them at matching volume. Phonetic coding of the produced speech audio was done manually for all participants. See supplementary materials for details.

### 2.3. Neural recordings

As part of the standard clinical DBS implantation procedure, functional mapping of the STN was performed with microelectrode recordings (MER) and LFPs were recorded from macroelectrode rings located 3 mm above the tip of the microelectrode (Alpha-Omega Engineering, Nof HaGalil, Israel). The microelectrodes were oriented on the microtargeting drive system using three trajectories of a standard cross-shaped Ben-Gun array with 2 mm center-to-center spacing (Central, Posterior, Medial), and referenced to the metal screw holding one of the guide cannulas used to carry the microelectrodes. Prior to initiating MER mapping, one or two high-density subdural electrocorticography (ECoG) strips with 54 or 63 contacts were placed through the standard burr hole, targeting the left superior temporal gyrus (covering also the ventral sensorimotor cortex) and left inferior frontal gyrus. Two or three sessions of the task were performed by each subject while the microelectrodes were

positioned at different depths within the STN. After the left DBS lead was successfully implanted, a final session of the speech task was performed by some participants, providing LFP data from DBS leads. ECoG and DBS lead recordings were acquired with a Grapevine Neural Interface Processor equipped with Micro2 Front Ends (Ripple LLC, Salt Lake City, UT, USA) and referenced to a sterile stainless-steel subdermal needle electrode placed on the scalp, approximately at the location of Cz in a standard EEG montage. Electrode localization was performed as previously described (Horn and Kuhn, 2015; Randazzo et al., 2016). See Supplementary Material and Table S1 for additional information.

The clinical setup evolved during the collection of this dataset, between subjects 22 and 23, transitioning from a traditional stereotactic frame to the use of robotic stereotactic assistance (Faraji et al., 2020). This change resulted in modification of the stereotactic frame's mechanical coupling to the electrode micro-drive.

#### 2.4. Vibration sensor

A shielded piezoelectric vibration sensor (model SDT1-028 K, TE Connectivity Company) was fixed to the stereotactic frame using a sticky pad for the duration of one experiment. This sensor was selected for its flat transfer function at frequencies above 30 Hz. The signal from the sensor was captured without amplification as an analog input to the Grapevine system.

#### 2.5. Electrophysiological data preprocessing

Data processing was performed using custom code based on the FieldTrip toolbox (Oostenveld et al., 2011) implemented in Matlab, available at ([github.com/Brain-Modulation-Lab/bml](https://github.com/Brain-Modulation-Lab/bml)). Recordings from the Grapevine, Neuro-Omega and Zoom-H6 systems were temporally aligned based on the stimulus and produced audio channels using a linear time-warping algorithm. Continuous alignment throughout the entire recording session was achieved with sub-millisecond precision. Data was low-pass filtered at 250 Hz using a 4th order non-causal Butterworth filter, down-sampled to 1 kHz and stored as continuous recordings in FieldTrip datatype-raw objects in mat containers. This frequency range is well-suited for analyses in the canonical frequency bands normally used to explore cognitive functions. All annotations, including descriptions of each session (duration, type of subcortical recording, depth of the MER recordings), details of the electrodes (active time intervals, channel names, coordinates in native and MNI space, anatomical labels), phonetic coding at the phoneme, syllable and triplet level, and times of stimulus presentation were stored in annotation tables.

An automatic data cleaning procedure was used to remove segments of data with conspicuous high-power artifacts. First, a 1 Hz high-pass 5th order non-causal Butterworth filter was applied to remove low frequency movement related artifacts. The power at frequencies in different canonical bands (3 Hz for  $\delta$ , 6 Hz for  $\theta$ , 10 Hz for  $\alpha$ , 21 Hz for  $\beta$ , 45 Hz for  $\gamma_L$  and 160 Hz for  $\gamma_H$ ) was estimated by convolution with a Morlet wavelet with a width parameter of 9. For each frequency, the maximum power in 1-s time bins was calculated, log-transformed and the mean ( $\bar{x}$ ) and standard deviations ( $\sigma$ ) of the distribution were estimated using methods robust to outliers. A time bin was defined as artifactual if its

maximal log-transformed power in any band exceeded  $\bar{x} + 3\sigma$  for that band. Note that this resulted in thresholds at least 10-fold higher than the mean power. Channels were entirely discarded if more than 50% of the time-bins were classified as containing artifacts. Blocks of channels sharing a headstage connector were entirely discarded if more than 50% of those channels were defined as artifactual.

For each trial, 3 different behavioral epochs were defined: stimulus presentation or listening epoch - the 1.5-s long window during which syllable triplets were presented auditorily; speech production epoch - the variable time during which subjects repeated the syllable triplet; baseline epoch - a 500-ms time window centered between speech offset of one trial and stimulus onset of the following.

## 2.6. Time-frequency plots

Time-frequency analyses for neural and audio data were performed using the Short Time Fourier Transform (STFT) method with a 100 ms Hanning window and a frequency step of 2 Hz, based on multiplication in the frequency domain as implemented by FieldTrip. Trials were aligned to speech onset and Z-scored relative to a 500-ms baseline epochs included in every trial. Frequencies up to 250 Hz were used for this analysis as that covers the canonical frequency bands normally used to explore cognitive functions.

## 2.7. Spectrogram correlation analysis

To index the degree of similarity between the audio spectrogram and the time-frequency spectrogram of a neural channel calculated by the STFT method, a correlation between these two matrices was calculated. This correlation was computed as the normalized sum of the element-by-element products of the two matrices.

$$r = \frac{\sum_m \sum_n (A_{m,n} - \bar{A})(B_{m,n} - \bar{B})}{\sqrt{\sum_m \sum_n (A_{m,n} - \bar{A})^2 \times \sum_m \sum_n (B_{m,n} - \bar{B})^2}}, \quad (1)$$

where A represents the audio spectrogram and B the time-frequency spectrogram of data at a given neural channel.

## 2.8. Coherence analysis

Phase relationship between the audio signal and the neural signal at a given channel was quantified using a metric of inter-trial phase consistency (ITPC) (Cohen, 2014). First, the audio and the neural signals were band-pass filtered between 70 and 240 Hz using a 5th order non-causal Butterworth filter. This frequency range contains the fundamental frequency of the voice in humans and the narrowband component studied in this work. A notch filter was applied to remove line noise and its harmonics. For each individual epoch of interest (noted by the index  $e$ ) and neural channel ( $X$ ), a complex value  $\varphi_e$  was calculated following

$$\varphi_e = \frac{1}{|X_e| |A_e|} \sum_k S_{e,k} A_{e,k}, \quad (2)$$

where  $S_e = X_e + iH(X_e)$  is the analytic signal,  $H(X_e)$  is the Hilbert transform of the neural data for the epoch  $e$ , and  $A_e$  is the audio signal for that epoch. The sum is taken for every sample  $k$  within the epoch.  $|X_e|$  and  $|A_e|$  are the Euclidean norms of the neural and audio signals for epoch  $e$ . The absolute value and phase of  $\varphi_e$  represents the degree of correlation and phase relationship between the neural and the audio channels for epoch  $e$ . If there is inter-trial phase consistency, the mean value of  $\varphi$  across trials (noted as  $\langle \varphi \rangle$ ) will be significantly different from 0. To quantify this, the ITPC index was defined as

$$ITPC = \frac{|\langle \varphi \rangle|}{StdErr(\varphi)}, \quad (3)$$

where the standard error of  $\varphi$  is defined as  $StdErr(\varphi) = \sqrt{\sum_e |\varphi_e - \langle \varphi \rangle|^2} / N$ , and the sum is taken over the  $N$  epochs considered for the neural channel of interest. Note that this metric was calculated independently for the speech production, listening and baseline epochs.

## 2.9. Significance threshold for coherence index

To define a threshold of significance for the coherence index, a Monte Carlo simulation was performed to obtain the distribution of coherence index under the null hypothesis of no consistent phase relationship between the neural and the audio channels. To this end, a random time jitter uniformly distributed between  $-100$  and  $100$  ms was applied to the neural data before calculating each  $\varphi_e$  value. 22,000 independent randomizations were calculated using data from all electrodes in the dataset. This analysis resulted in a significant threshold for the coherence index of 3.08 that corresponds to the 99.99 percentile of the distribution. Thus, a coherence index greater than 3.08 suggests significant correlation of inter-trial phase consistency between the audio and the neural signal.

## 2.10. Objective assessment of acoustic contamination

A recent study by Roussel et al. (2020), comparing intracranial recordings collected from human subjects during speech perception and production at five different research institutions found that spectrotemporal features of the recorded neural signal are highly correlated with those of the sound produced by the participants or played to participants through a loudspeaker. The method proposed by Roussel et al. for quantifying the extent of acoustic contamination in an electrophysiological recording was applied to the data using the open source toolbox developed by the authors (Roussel et al., 2020) (<https://doi.org/10.5281/zenodo.3929296>). Briefly, the method correlates the power of the neural data and audio across different frequency bins, thus creating a correlation matrix for every combination of frequencies of the two channels. Significantly higher correlation coefficients at matching frequencies of the two channels (i.e., on the diagonal of the matrix), compared to non-matching frequencies, are considered to be evidence of acoustic contamination. A permutation test is used to determine the significance threshold. The method was applied to data from individual electrodes, and the False Discovery Rate was adjusted according to (Benjamini and Hochberg, 1994).

### 2.11. Testing the spatial distribution of coherence over the brain

We used hierarchical bootstrapping (Saravanan et al., 2020) to test whether any particular brain region displayed an average coherence that was significantly different from the rest of the brain. Specifically, we built a null distribution of average coherence across brain regions by calculating the mean coherence accounting for subjects as one hierarchical level but ignoring brain regions within subjects. We then calculated the average coherence for the 15 brain regions (as parcellated by the MMP1 atlas) that had coverage in 10 or more subjects, with 3 or more electrodes per subject. Each distribution was built using subjects as the hierarchical level and electrodes were restricted to those within that particular brain region. Bootstrapping was performed weighing each subject by the number of electrodes present in that region. The distributions were then all compared to the null distribution and the significance threshold was adjusted using an FDR correction for 15 comparisons. Resampling number was set to 10,000 for all bootstrap samples.

## 3. Results

### 3.1. Narrowband high gamma component in neural recordings during speech production

We averaged spectrograms time-locked to the speech onset across trials for each audio and neural channel. Representative examples of the averaged spectrograms for each recording type are provided in Fig. 2. Fig. 2A shows the spectrogram for the produced audio, in which the fundamental frequency (F0) of the participant's voice (at around 120 Hz) and its first harmonic (at around 240 Hz) can be easily discerned as an increase in power at the corresponding frequencies. The 3 peaks of power in the spectrogram at different times correspond to the three produced syllables. A similar narrowband component occurring around the frequencies of the participants' F0 also appeared in some electrodes during the speech production epoch. For example, this narrowband component can be readily observed in the time-frequency plot for one ECoG electrode shown in Fig. 2B, but not for another ECoG electrode from the same subject shown in Fig. 2C. Thus, while both electrodes show an increase in speech-related gamma activity, the increase in gamma activity in the electrode in Fig. 2B is remarkably similar to the narrowband component in the audio spectrogram (Fig. 2A), overlapping with it in frequency, time, and overall shape. Similar narrowband components in the high gamma frequency range were also identified in some of the LFP recordings extracted from the micro electrodes (Fig. 2D), macro electrodes (Fig. 2E) and from the DBS leads (Fig. 2F). Thus, this narrowband speech-related component can be observed in different electrophysiological recordings collected simultaneously with different acquisition devices. Furthermore, this narrowband component can co-occur with speech-related broadband gamma activity as shown in Fig. S1.

### 3.2. The narrowband high gamma component correlates with the fundamental frequency of the voice

Because of the striking similarity between the neural data and speech spectrogram, we set out to quantify the identified narrowband high gamma component and its relationship with the produced audio further, using different analytical approaches. First, we asked whether the observed overlap in the frequency range between the narrowband component and the produced speech audio was consistent across participants. To this end, we calculated the

Welch power spectrum of the audio and neural data during the speech production epochs (Fig. 3A), identified at which frequencies peak power within the F0 range (70–240 Hz) occurs in both types of spectra, and correlated the obtained frequency values. For each subject, we used data from single trials of the LFP signal extracted from one of the micro channels of the subcortical mapping electrodes, selected for having a prominent narrowband high gamma component.

As can be seen in Fig. 3B, there is a strong correlation (Spearman's  $\rho=0.98$ ,  $p$ -value  $< 10^{-6}$ , intercept =  $1.4\pm 5.1$  Hz, slope =  $0.99\pm 0.4$ ) between the fundamental frequency of the voice and the peak frequency of the narrowband component across participants. Furthermore, the relation not only is linear, but also has a slope not significantly different from 1, meaning that the frequency of peak high gamma power in the neural data corresponds to the fundamental frequency of the voice.

### 3.3. Spectrogram cross-correlation between audio and neural data

To further characterize the distribution of this narrowband component across electrodes and recording sessions, we developed two different and complementary measures of similarity between the neural signal and the audio signal. The first metric consists of correlating the time-frequency spectrogram of a neural channel across times and frequencies with the spectrogram of the produced audio. A schematic representation of the method is shown in Fig. 4A. For each subject, the correlation coefficient between the spectrogram of the produced audio and the spectrogram of neural recordings was calculated (Eq. (1)). We found widespread correlation between spectrograms obtained from intracranial recordings and spectrograms of the produced audio, reaching correlation coefficients of up to 0.8 (Fig. 4B). The strength of correlations was variable across subjects, recording sessions, and electrodes. Also note that strong correlations were present in different types of intracranial recordings, albeit with a varying consistency.

### 3.4. Consistent phase relationship between audio and neural data

The method described above compares similarity of time-frequency resolved *power* between neural and audio data but does not take into account the phase information of the signals. Therefore, we developed a complementary metric to quantify the *phase* relationship between the neural data and the produced audio, that is, a measure of coherence or inter-trial phase consistency (ITPC) with the produced audio. This metric is based on dot products of the analytic signal of the neural channel and the produced audio, as schematized in Fig. 5A. For each epoch, a complex value representing the magnitude of the correlation and the phase relationship of the neural signal with the audio is obtained (Eq. (2)) If the mean of these complex values is significantly different from zero, this serves as evidence of a consistent phase relationship between the neural data and the produced speech (Fig. 5B). We used the absolute value of the mean of these complex values, normalized by their standard error, as an index of coherence (Eq. (3)). This method is computationally efficient and well suited for narrowband signals as the one characterized here. We calculated a significance threshold using a Monte Carlo simulation in which we applied random time jitters before calculating the coherence index (see details in Methods Section).

As observed in Fig. 5C, there is widespread coherence across many subjects and all electrode types during the speech production epoch. Around 50% of the analyzed electrodes show significant coherence with the audio during the speech production epoch (Table 1). Importantly, no significant coherence with the speech audio was observed during the baseline or listening epochs (Table 1). Coherence of the neural signals with the stimulus audio in all behavioral epochs, including the listening epoch, was negligible (Table 1). This suggests that only production of speech sounds was contaminating the neural signal.

The distribution of the coherence indices across electrodes for each recording session can be classified as (i) having no or little coherence between neural channels and the produced speech (e.g., subjects 06, 03, 21); (ii) having homogenous coherence across electrodes, (e.g., subjects 02, 04); and (iii) having heterogeneous coherence across electrodes (e.g., subjects 14, 28). While for the homogeneous case both the amplitude of the coherence ( $|\langle\phi\rangle|$ ) and the phase relationship with the produced speech are similar across the neural electrodes, in the heterogeneous recording sessions these values may change substantially across electrodes (Fig. 5D).

Our syllable triplet repetition task contained trials cued at either low or high volume, and participants were instructed to repeat them aloud at matching intensity. All but two of the participants achieved significant modulation of their voice intensity as assessed by measuring the sound pressure level (SPL, relative to background noise) during production of vowels (Fig. S2A). The distributions of SPL for high and low trials significantly overlapped and the mean difference between these conditions ranged from 1 to 5 dB for most participants (Fig. S2A). Neural recordings from participants that achieved modulation of their voice intensity showed significant differences in their coherence with the audio between high and low trials in 88% of the cases (Fig. S2B). We were unable to correlate the prevalence of the artifact to the absolute speech volume across participants due to the lack of an absolute volume calibration of the microphone.

### 3.5. The speech acoustic component can be detected in the neural data by different quantification methods

The spectrogram correlation index (Fig. 4) and the coherence index (Fig. 5) are highly correlated with each other, as can be observed in Fig. 6A (Spearman's  $\rho = 0.7$ ,  $p < 1e-6$ ). In applying the method proposed by Roussel et al. (2020), the power of the neural data was correlated with the audio across different frequency bins to create a correlation matrix (Fig. 6B). High correlation coefficients on the diagonal of this matrix indicate acoustic contamination (see details in the Methods Section). Electrodes classified as contaminated based on this method are indicated by red triangles in Fig. 6A. As can be observed, these points tend to have high spectrogram correlation index and coherence index above the significant threshold (Fig. 6A). This result suggests that the spectrogram correlation index, the coherence index, and the method developed by Roussel et al. have similar sensitivity in identifying speech-related artifacts in our dataset.

### 3.6. Coherence indices are independent of anatomic location

Next, we asked if there is any spatial structure of the coherence index. To this end, we performed a hierarchical bootstrapping analysis accounting for the nested nature of the data (electrodes within anatomical regions within subjects) and found that none of the regions (as defined by the Multi Modal Parcellation 1 in Glasser et al. (2016)) show values of coherence significantly higher than the average distribution over the entire brain (see methods for detail). All cortical electrodes with their corresponding coherence values are plotted on a standard brain in Fig. 7A. Electrodes with high coherence with the produced audio do not cluster on any specific neuroanatomical region. Similarly, no spatial clustering of the coherence index can be observed in the STN from micro-electrode recordings (Fig. 7B), recordings from the macro rings situated 3 mm above the tip of the micro-electrodes (Fig. 7C) or from DBS leads recordings (Fig. 7D).

### 3.7. Speech-related vibrations can be detected in non-neural data

The experiments described above demonstrated that some neural recordings show time-frequency patterns similar to the produced audio recordings. This suggests that there is contamination of the electrophysiological neural data with the speech audio signal. If this is the case, we expect to find the same kind of contamination in "blank" electrodes not in contact with the brain. Most of the ECoG strips used in our experiments contained 63 contacts laid out in a  $3 \times 21$  arrangement (Fig. 8A). These contacts were connected to the amplifier's front-end through 4 cabrio-type connectors, each containing 16 pins. This resulted in the last pin of the 4th cabrio connector (#64) not connected to any electrode on the brain. Instead, the wire connected to this pin runs the length of the cable and ends within the silicon rubber matrix of the ECoG strip. We recorded the signal from this "blank" pin as it provides a control for non-neural sources of noise affecting the neural signal. Using the same time-frequency method as before, we analyzed the recorded signal from this blank ECoG headstage pin. As can be observed in Fig. 8B, a narrowband component similar to that observed in some neural recordings is also present during speech production in the recordings from the blank headstage pin. It is interesting to note that the frequency of peak power recorded from this pin is slightly lower than the fundamental frequency of the voice (Fig. 8C), although the component has the same timing and overall pattern (note the power increase around the first harmonic of the F0). As shown in the bottom row of the Fig. 5C, labeled 'Blank', signals from the blank headstage pins show significant coherence with the produced speech audio in the same recording sessions that showed strong coherence with the produced speech audio in other electrode types (see also Fig. 4B and Table 1).

These results strongly suggest that the source of the observed narrowband component is not neural. Among possible sources of this component are speech-induced vibrations of the stereotactic frame, cables, connectors and/or acquisition chain. To address this question, we attached a piezoelectric vibration sensor to the stereotactic frame (Fig. 8D) during data collection in one subject (subject DBS3029). The recorded signal from the piezoelectric sensor was analyzed in the same way as other types of recordings. A strong narrowband component was observed at the time corresponding to the production of the first syllable, in the same frequency range as the fundamental frequency of the voice (Fig. 8E). The attenuated power observed during the time of the production of the second and the third

syllables might be due to the fact that in this particular participant speech intensity decreased across the produced syllable triplet, as seen in the audio spectrogram in Fig. 8F.

#### 4. Discussion

We identified the presence of a narrowband high gamma component in the neural signals recorded from patients undergoing DBS implantation surgery that is consistent with a mechanically induced artifact. This component is widespread across many electrode types and is the most prominent feature in many electrode recordings. It occurs almost exclusively during cued speech production epochs and it has spectral and temporal characteristics strikingly similar to the produced speech audio. Indeed, a recent work shows the presence of acoustic contamination in ECoG recordings (Roussel et al., 2020). In the environment of DBS surgery, speech-induced vibrations conducted by the skull and stereotactic frame can impinge on the electrodes and/or signal acquisition chain affecting the recorded signal.

Several results support the interpretation that the observed narrowband high gamma component is an artifact due to speech-induced vibrations. First, the frequency of peak power of the narrowband component tracks the fundamental frequency of the voice across participants (Fig. 3). Second, the narrowband high gamma component is almost exclusively present during the cued speech production epoch, but not the listening epoch (Table 1). Thirdly, the time-frequency resolved power from the neural recordings strongly correlates with the produced audio spectrogram (Fig. 4). Fourth, significant inter-trial phase consistency between the produced audio and the neural data suggests similarities not only across the frequency domain, but also the temporal domain (Fig. 5). Fifth, most of the recordings that we classified as contaminated in our analysis were also classified as having acoustic contamination by the recently proposed method in Roussel et al. (2020) (Fig. 6 and Table 1). Sixth, there was no significant cortical localization of the coherence index (Fig. 7). Finally, the narrowband high gamma component was also detected in "blank" pins of the headstage connector not connected to any electrode (Fig. 8B) and in the recording from a vibration sensor attached to the stereotactic frame (Fig. 8E). Taken together, these results strongly suggest the presence of speech-induced vibration artifact.

Although we cannot rule out the presence of physiological neural activity with the exact same spectral and timing characteristics as the observed narrowband high gamma component, we favor the interpretation that the narrowband component identified in this work is mainly, if not completely, due to the vibration artifact. It is worth mentioning that broadband gamma activity can be detected in many electrodes (see example in Fig. 2C), including some that also show the vibration artifact (see Fig. S1D).

These results are in line with a recent report by Roussel et al. (2020), in which the authors show evidence for acoustic contamination of ECoG recordings. The authors analyze multiple-center datasets collected in epilepsy patients in an extra-operative setting, finding that both produced and stimulus audio can affect ECoG recordings. Our work extends these findings, showing that the same kind of contamination can occur not only in the ECoG recordings, but can also affect other types of invasive neural recordings, such as those collected in the context of DBS implantation surgery. In addition, there are two key

differences to note between our results and those of Roussel et al. First, we only observe contamination when the patient is speaking, but not during auditory stimulus presentation. This difference may be due to the use of headphones in our recording setup as opposed to the use of loudspeaker in the work by Roussel et al., who found that acoustically isolating the speaker by placing it in a soundproof box reduced contamination of the neural signal. Second, in our recordings the affected signals are those corresponding to the F0 and to a lesser extent its harmonics. This could be explained by the fact that the stereotactic frame imposes some additional mechanical constraints, thus changing the way the vibration propagates.

Even though intracranial recordings in general are less prone to artifacts than extracranial recordings, it is recognized that the patient's speech induces vibrations that affect MER. For example, a patent for a new micro-electrode design from AlphaOmega mentions that "*various mechanical, noise and vibration, such as motor vibration, motion of the electrode within the tissue or voice of the subject, are detected by the electrode that acts essentially as microphone and is erroneously combined with the neural signal that is being recorded*" (Alpha Omega Technologies, 2020). Therefore, a common practice has been to analyze the recordings only when the patient is not speaking. The introduction of "microphonic free" microelectrodes with improved shielding that reduces the effects of vibrations on the recordings, allows acquiring single unit activity while the patient is speaking (Alpha Omega Technologies, 2020). Besides the clear clinical advantage, this has opened the possibility of studying single unit activity of DBS target structures during speech production. Although the quantifications of single-unit firing can be reliably performed with these electrodes (Lipski et al., 2017, 2018), in light of our results it is clear that mechanical vibrations affect other intracortical recordings including those obtained with macro contacts on the shaft of the micro electrodes, recordings from ECoG strips and recordings from the clinically implanted DBS leads.

Interestingly, neural signals with similar characteristics to the narrowband high gamma component described in this work have been reported in the literature. The Frequency Following Response (FFR) in the auditory brainstem is a potential with spectrotemporal features resembling the stimulus audio that reflects sustained neural ensemble activity phase-locked to periodic acoustic stimuli (Bidelman, 2018; Marsh and Worden, 1968; Marsh et al., 1970; Rose et al., 1966). This brainstem response to auditory stimuli can be recorded from scalp electrodes by averaging over hundreds of trials, a technique that has become a powerful diagnostic tool in audiology and neurology known as the Auditory Brainstem Response (Hall, 1992; Jewett et al., 1970). In recent years several works based on scalp EEG, sEEG and MEG have reported cortical FFRs (Behroozmand et al., 2016; Bidelman, 2018; Coffey et al., 2016).

In our data, there are two features that argue against the narrowband component being a true FFR. First, it only occurs during speech production and not during auditory stimulus presentation. Second, the narrowband artifact is not localized to the auditory cortex, or to any other cortical region (Fig. 7). In light of the results presented in this work and similar results recently published by Roussel et al, it is clear that caution should be taken when interpreting cortical FFR, due to the fact that this signal is exactly what would be expected

if there was an artifact (e.g., vibration at electrodes or connectors, electromagnetic induction by speakers, electrical crosstalk in the amplifier or connectors).

Other reported sources of artifacts affecting intracranial recordings, including artifacts due to eye blinking (Ball et al., 2009) and other facial muscle contraction (Otsubo et al., 2008), have spectral characteristics distinct from the narrowband component described in this work; they show broadband spectrums that do not match that of the produced audio and are not expected to track the fundamental frequency of the voice or correlate with the power of the speech audio across time.

Acknowledging the existence of this speech-induced vibration artifact is an important first step to avoid overinterpreting spurious features of the data. Many important questions related to high-level cognitive processes, including the neural control of speech production, can only be answered by acquiring recordings that are likely to be affected by the described artifact, but several steps can be taken to identify it. First, methods that correlate the audio signal with the neural data can be used to detect the presence of acoustic contaminations. Second, recording from open headstage pins provides a control for non-neural sources affecting the signal. Third, vibration sensors can detect mechanical vibrations along the recording system that might affect the signal.

We observed marked heterogeneity in the magnitude of the artifact across subjects and, in some cases, between recording sessions for the same subject (Figs. 4 and 5). The time between consecutive recording sessions was of several minutes up to an hour, during which significant surgical events took place, like removing the mapping electrodes and implanting the DBS leads, repositioning of interconnector cables and irrigating the brain through the burr hole. These changes can influence the way the vibration artifact affects the recordings. We also observed significant spatial heterogeneity of this speech-induced vibration artifact across electrodes, suggesting that data-driven referencing schemes could be investigated as a method to remove this artifact from intracranial recordings.

Identifying and mitigating artifacts in intracranial recordings from awake patients is fundamental to achieving reliable and reproducible results in the field of human systems neuroscience. This, in turn, will lead to an improved understanding of the neural physiology and pathophysiology of uniquely human cognitive abilities.

## Supplementary Material

Refer to Web version on PubMed Central for supplementary material.

## Acknowledgments

We would like to thank all participants of this study for their time and effort. We would also like to thank Robert S. Turner for suggestions on data analysis. This work was funded by the National Institute of Health (BRAIN Initiative), through grants U01NS098969, U01NS117836 and R01NS110424 to R.M.R.

## References

Alpha Omega Technologies. (2020). Reduced Larsen Effect Electrode.

- Anumanchipalli GK, Chartier J, Chang EF, 2019. Speech synthesis from neural decoding of spoken sentences. *Nature* 568, 493–498. [PubMed: 31019317]
- Ball T, Kern M, Mutschler I, Aertsen A, Schulze-Bonhage A, 2009. Signal quality of simultaneously recorded invasive and non-invasive EEG. *Neuroimage* 46, 708–716. [PubMed: 19264143]
- Behroozmand R, Oya H, Nourski KV, Kawasaki H, Larson CR, Brugge JF, Howard MA, Greenlee JDW, 2016. Neural correlates of vocal production and motor control in human Heschl’s gyrus. *J. Neurosci* 36, 2302–2315. [PubMed: 26888939]
- Benjamini Y, Hochberg Y, 1994. Controlling the false discovery rate: a practical and powerful approach to multiple testing. *J. R. Stat. Soc. Ser. B* 57 (1), 289–300 (Methodological)
- Bidelman GM, 2018. Subcortical sources dominate the neuroelectric auditory frequency-following response to speech. *Neuroimage* 175, 56–69. [PubMed: 29604459]
- Bouchard KE, Mesgarani N, Johnson K, Chang EF, 2013. Functional organization of human sensorimotor cortex for speech articulation. *Nature* 495, 327–332. [PubMed: 23426266]
- Cheung C, Hamiton LS, Johnson K, Chang EF, 2016. The auditory representation of speech sounds in human motor cortex. *Elife* 5, e12577. [PubMed: 26943778]
- Chrabaszcz A, Neumann W-J, Stretcu O, Lipski WJ, Bush A, Dastolfo-Hromack CA, Wang D, Crammond DJ, Shaiman S, Dickey MW, et al. , 2019. Subthalamic nucleus and sensorimotor cortex activity during speech production. *J. Neurosci* 39, 2698–2708. [PubMed: 30700532]
- Coffey EBJ, Herholz SC, Chepesiuk AMP, Baillet S, Zatorre RJ, 2016. Cortical contributions to the auditory frequency-following response revealed by MEG. *Nat. Commun* 7, 11070. [PubMed: 27009409]
- Cohen MX, 2014. *Analyzing Neural Time Series Data*. MIT Press.
- Conant DF, Bouchard KE, Leonard MK, Chang EF, 2018. Human sensorimotor cortex control of directly measured vocal tract movements during vowel production. *J. Neurosci* 38, 2955–2966. [PubMed: 29439164]
- Crone NE, Hao L, Hart J, Boatman D, Lesser RP, Irizarry R, Gordon B, 2001. Electrographic gamma activity during word production in spoken and sign language. *Neurology* 57, 2045–2053. [PubMed: 11739824]
- Edwards E, Nagarajan SS, Dalal SS, Canolty RT, Kirsch HE, Barbaro NM, Knight RT, 2010. Spatiotemporal imaging of cortical activation during verb generation and picture naming. *Neuroimage* 50, 291–301. [PubMed: 20026224]
- Faraji AH, Kokkinos V, Sweat JC, Crammond DJ, Richardson RM, 2020. Robotic-assisted stereotaxy for deep brain stimulation lead implantation in awake patients. *Oper. Neurosurg* 19, 444–452.
- Flinker A, Korzeniewska A, Shestyk AY, Franaszczuk PJ, Dronkers NF, Knight RT, Crone NE, 2015. Redefining the role of Broca’s area in speech. *Proc. Natl. Acad. Sci* 112, 2871–2875. [PubMed: 25730850]
- Flinker A, Piai V, Knight RT, 2018. Rueschemeyer SA; Gaskell MG (ed.),. In: *The Oxford Handbook of Psycholinguistics*. Oxford University Press, NY, pp. 992–1010 2dn ed..
- Fonov V, Evans AC, Botteron K, Almli CR, McKinstry RC, Collins DLthe Brain Development Cooperative Group, 2011. Unbiased average age-appropriate atlases for pediatric studies. *Neuroimage* 54 (1), 313–327. [PubMed: 20656036]
- Glasser MF, Coalson TS, Robinson EC, Hacker CD, Harwell J, Yacoub E, Ugurbil K, Andersson J, Beckmann CF, Jenkinson M, et al. , 2016. A multi-modal parcellation of human cerebral cortex. *Nature* 536, 171–178. [PubMed: 27437579]
- Hall JW, 1992. *Handbook of Auditory Evoked Responses*. Allyn & Bacon, MA, USA Allyn & Bacon.
- Hamilton LS, Edwards E, Chang EF, 2018. A spatial map of onset and sustained responses to speech in the human superior temporal gyrus. *Curr. Biol* 28, 1860–1871 e4. [PubMed: 29861132]
- Horn A, Kühn AA, 2015. Lead-DBS: a toolbox for deep brain stimulation electrode localizations and visualizations. *Neuroimage* 107, 127–135. [PubMed: 25498389]
- Jewett DL, Romano MN, Williston JS, 1970. Human auditory evoked potentials: possible brain stem components detected on the scalp. *Science* 167 (3924), 1517–1518. [PubMed: 5415287]
- Lachaux JP, Rudrauf D, Kahane P, 2003. Intracranial EEG and human brain mapping. *J. Physiol Paris* 97, 613–628.

- Lipski WJ, Wozny TA, Alhourani A, Kondylis ED, Turner RS, Crammond DJ, Richardson RM, 2017. Dynamics of human subthalamic neuron phase-locking to motor and sensory cortical oscillations during movement. *J. Neurophysiol* 118, 1472–1487. [PubMed: 28592690]
- Lipski WJ, Alhourani A, Pirmia T, Jones PW, Dastolfo-Hromack C, Helou LB, Crammond DJ, Shaiman S, Dickey MW, Holt LL, et al. , 2018. Subthalamic nucleus neurons differentially encode early and late aspects of speech production. *J. Neurosci* 38, 5620–5631. [PubMed: 29789378]
- Llorens A, Trébuchon A, Liégeois-Chauvel C, Alario F-X, 2011. Intra-cranial recordings of brain activity during language production. *Front. Psychol* 2, 375. [PubMed: 22207857]
- Marsh JT, Worden FG, 1968. Sound evoked frequency-following responses in the central auditory pathway. *Laryngoscope* 78, 1149–1163. [PubMed: 5659588]
- Marsh JT, Worden FG, Smith JC, 1970. Auditory frequency-following response: neural or artifact? *Science* 169, 1222–1223. [PubMed: 5450700]
- Martin S, Millán JDR, Knight RT, Pasley BN, 2019. The use of intracranial recordings to decode human language: challenges and opportunities. *Brain Lang.* 193, 73–83. [PubMed: 27377299]
- Mesgarani N, Cheung C, Johnson K, Chang EF, 2014. Phonetic feature encoding in human superior temporal gyrus. *Science* 343, 1006–1010. [PubMed: 24482117]
- Moses DA, Metzger SL, Liu JR, Anumanchipalli GK, Makin JG, Sun PF, Chang EF, 2021. Neuroprosthesis for decoding speech in a paralyzed person with anarthria. *N. Engl. J. Med* 385 (3), 217–227. [PubMed: 34260835]
- Mugler EM, Tate MC, Livescu K, Templer JW, Goldrick MA, Slutzky MW, 2018. Differential representation of articulatory gestures and phonemes in precentral and inferior frontal gyri. *J. Neurosci* 38, 9803–9813. [PubMed: 30257858]
- Mukamel R, Fried I, 2012. Human intracranial recordings and cognitive neuroscience. *Annu. Rev. Psychol* 63, 511–537. [PubMed: 21943170]
- Oostenveld R, Fries P, Maris E, Schoffelen J-M, 2011. FieldTrip: open source software for advanced analysis of MEG, EEG, and invasive electrophysiological data. *Comput. Intell. Neurosci.* 156869 2011 [PubMed: 21253357]
- Otsubo H, Ochi A, Imai K, Akiyama T, Fujimoto A, Go C, Dirks P, Donner EJ, 2008. High-frequency oscillations of ictal muscle activity and epileptogenic discharges on intracranial EEG in a temporal lobe epilepsy patient. *Clin. Neurophysiol* 119, 862–868. [PubMed: 18289931]
- Panov F, Levin E, Hemptinne C, de Swann NC, Qasim S, Miocinovic S, Ostrem JL, Starr PA, 2017. Intraoperative electrocorticography for physiological research in movement disorders: principles and experience in 200 cases. *J. Neurosurg* 126, 122–131. [PubMed: 26918474]
- Randazzo MJ, Kondylis ED, Alhourani A, Wozny TA, Lipski WJ, Crammond DJ, Richardson RM, 2016. Three-dimensional localization of cortical electrodes in deep brain stimulation surgery from intraoperative fluoroscopy. *Neuroimage* 125, 515–521. [PubMed: 26520771]
- Rose JR, Brugge JF, Anderson DJ, Hind JE, 1966. Phase-locked response to low-frequency tones in single auditory nerve fibers of the squirrel monkey. *J. Neurophysiol* 30 (4), 769–793.
- Roussel P, Godais GL, Bocquelet F, Palma M, Hongjie J, Zhang S, Giraud AL, Mgevand P, Miller K, Gehrig J, et al. , 2020. Observation and assessment of acoustic contamination of electrophysiological brain signals during speech production and sound perception. *J. Neural Eng* 17, 056028. [PubMed: 33055383]
- Saravanan V, Berman GJ, and Sober SJ (2020). Application of the hierarchical bootstrap to multi-level data in neuroscience. *Arxiv*.
- Sisterson ND, Carlson AA, Rutishauser U, Mamelak AN, Flagg M, Pouratian N, Salimpour Y, Anderson WS, Richardson RM, 2021. Electrocorticography during deep brain stimulation surgery: safety experience from 4 centers within the national institute of neurological disorders and stroke research opportunities in human consortium. *Neurosurgery* 88 (5), E420–E426. [PubMed: 33575799]

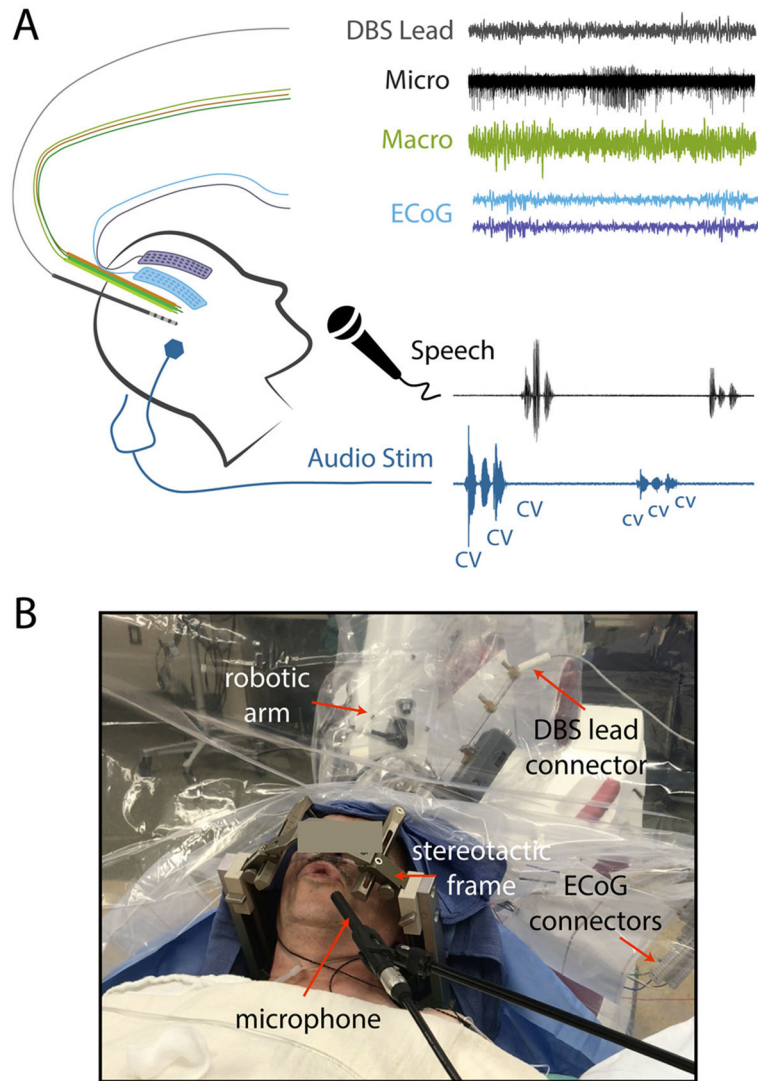


**Fig. 1.** Intraoperative intracranial recording setup and speech task. **A.** Schematic representation of intracranial electrodes and syllable triplet repetition task. During the mapping phase of the DBS implantation surgery ECoG strips were temporarily placed through the burr hole, allowing simultaneous recording of cortical and subcortical LFPs and MER from the STN. Participants were instructed to repeat aloud CV syllable triples at a volume matching the auditory stimuli. **B.** Photograph of a participant performing the speech task.

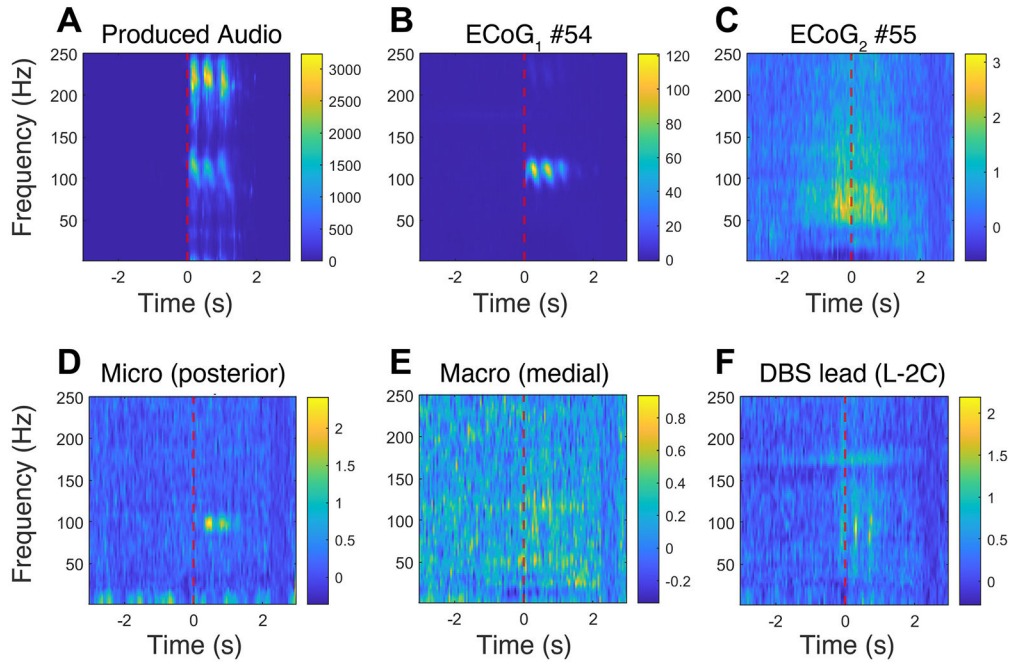


**Fig. 2.** A speech-related narrowband component in the high gamma frequency range was observed across different types of neural recordings. Time-frequency plots for the audio and different neural channels from subject DBS3014. The red vertical dashed line represents speech onset time, which was used to time-lock the data across trials. A. Average spectrogram of the produced speech audio, z-scored to baseline. B. ECoG strip 1 contact #54, showing a prominent narrowband high gamma component during the speech production epoch. C. ECoG strip 2 #55, showing a broadband activation during speech production (note that this activity begins before speech onset). D. Spectrogram for LFP signal extracted from the posterior micro electrode targeting the left STN. E. Spectrogram for LFP signal from the medial macro ring targeting the left STN. F. Spectrogram for the left DBS lead contact. Colorbars indicate scale of the z-scored spectral power for each panel.

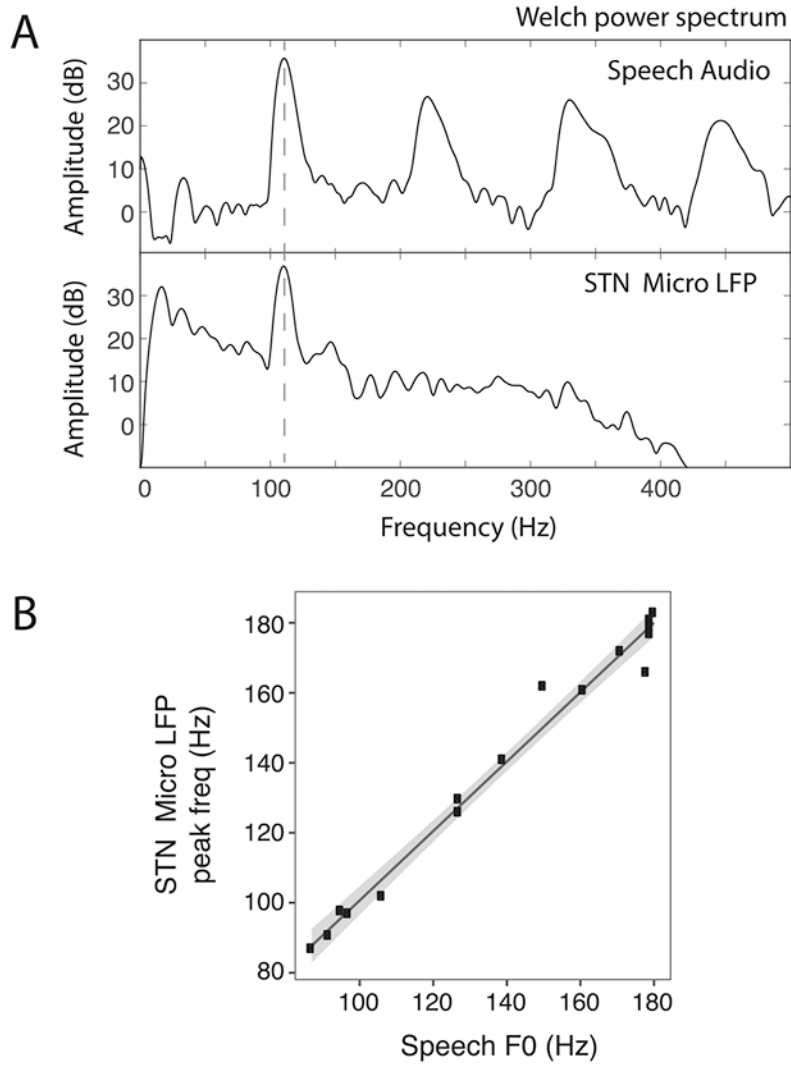


**Fig. 3.** The frequency of peak power of the high gamma narrowband component correlates with the fundamental frequency of the voice across participants. A. Welch power spectrums for the produced speech audio (top) and the LFP signal extracted from the micro tip of the subcortical mapping electrode by low-pass filtering at 400 Hz (bottom). The vertical dashed line represents the frequency of peak power identified in each spectrum. B. Correlation of the frequency of peak power in the range of 70–200 Hz between the audio and neural data. The solid line represents the best linear fit to the data; gray ribbon represents the confidence interval of the fit.

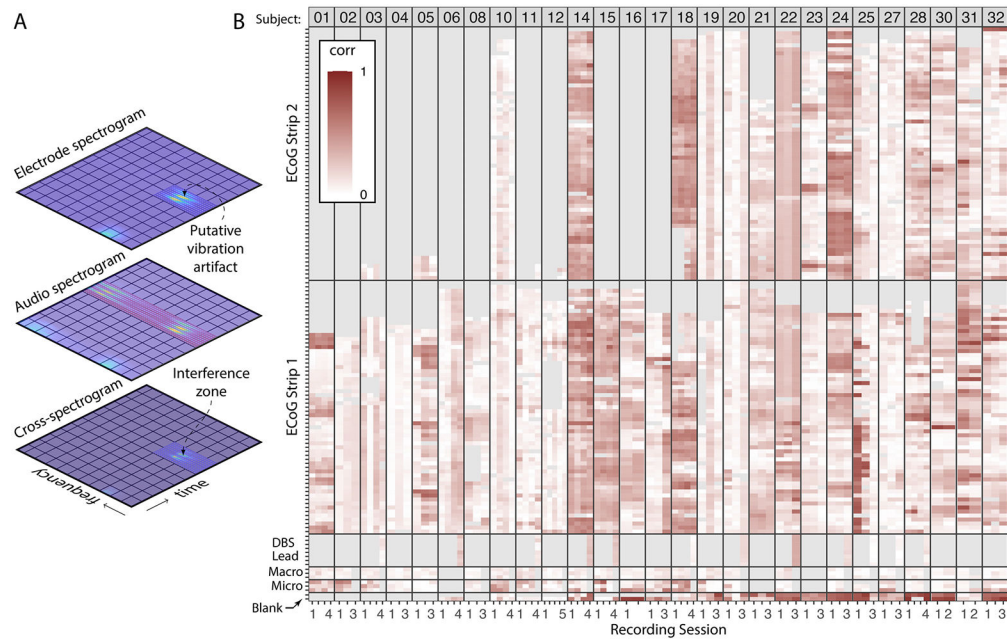


**Fig. 4.** Spectrogram correlation between audio and neural data. A. A schematic representation of the spectrogram correlation approach. The electrode spectrogram (top) is multiplied by the audio spectrogram (middle) to give the cross-spectrogram (bottom). B. Distribution in the dataset of the power correlation with the audio for all neural recordings. The degree of correlation is color-coded in red; each pixel represents one electrode (y-axis) in one recording session (x-axis). Panels are defined by subject (organized in columns labeled 1 to 32) and electrode type (organized in rows). ECoG strips are indicated by implantation order, with strip 1 targeting the STG and strip 2 targeting the IFG. Pixels in gray correspond to electrodes removed during artifact rejection or which were not available for a given session (e.g., ECoG strip 2 was not used in all subjects and recordings from the DBS leads were only acquired in the last session for a subset of subjects)

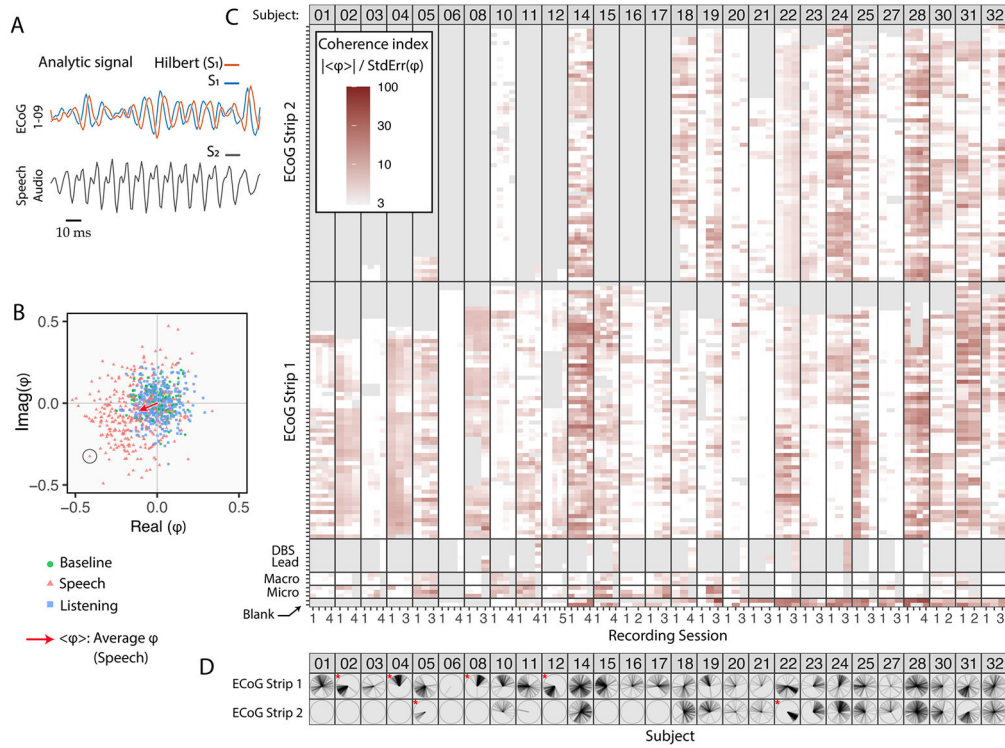


**Fig. 5.**

Inter-trial phase consistency (ITPC) reveals significant coherence of neural data with the produced speech audio. A coherence index is derived from multiplying the band-pass filtered analytic neural signal (blue and orange lines for real and imaginary parts, respectively) with the produced speech signal (black line) using the internal product, resulting in a complex value  $\varphi$  for each trial. B. An example of  $\varphi$  values plotted on the complex plane for three behavioral epochs: baseline (green circles), listening (blue squares), and speech production (red triangles). The coherence index is related to the average value of  $\varphi$ ,  $\langle \varphi_e \rangle$ , represented as a red arrow for the speech production epoch. For the baseline and listening epochs  $\langle \varphi_e \rangle$  approaches zero, indicating no coherence. The circled point corresponds to the traces shown in panel A. C. Coherence indices from the speech production epoch plotted for each electrode, recording session, and subject (as in Fig. 4B). The color of each pixel represents the coherence index for an electrode in each recording session. Electrodes are organized by type in the y-axis and sessions are organized by subject in the x-axis. Pixels in gray correspond to electrodes that were not present in the montage, or which were removed during artifact rejection. White pixels represent recordings that do not show significant coherence with the audio. ECoG strips are indicated by implantation order, with strip 1 targeted to the STG and strip 2 targeted to the IFG. D. Phase consistency of the neural data with the produced audio across contacts of the ECoG strips. In each polar plot, the angle between the radial lines and the horizontal axis represents the phase relation with the produced audio of an ECoG electrode. Red asterisks mark ECoG strips with homogeneous coherence, defined as those with at least 90% of the electrodes' phases within 90° of each other

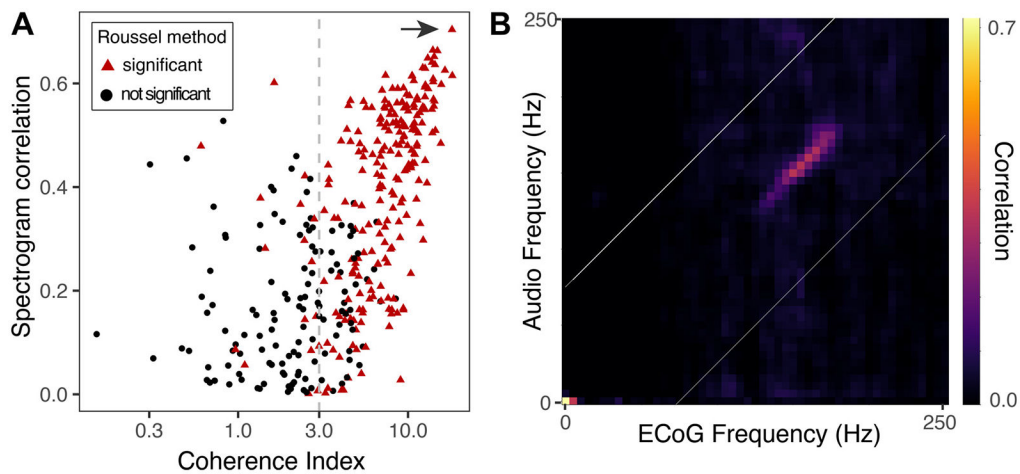


**Fig. 6.** The spectrogram correlation index and the coherence index show strong correlation with each other and high consistency with the Roussel et al. (2020) method’s outcome. A. Relationship between the spectrogram correlation index and the coherence index for ECoG electrodes for one representative subject (DBS3024). Red triangles indicate electrodes with significant ‘acoustic contamination’ as assessed by the method developed by Roussel et al. (2020). B. Detection of acoustic contamination by the Roussel method is based on the cross-frequency correlation matrix, which indicates degrees of correlation of power across time for different frequencies of the neural and audio data. The shown matrix corresponds to ECoG electrode 2–31, indicated by an arrow in panel A

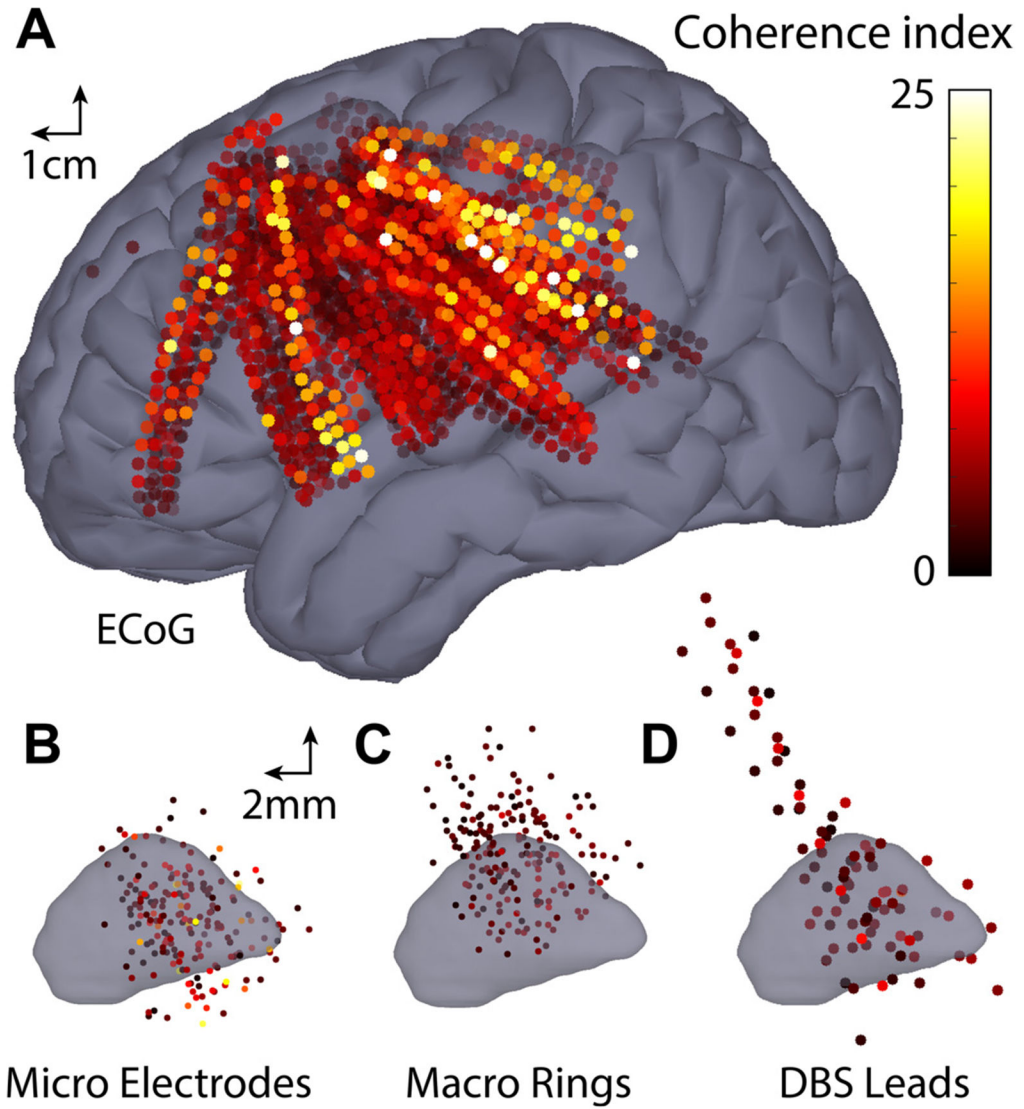


**Fig. 7.** Increased Inter-trial Phase Consistency is not specific to any anatomical region. A. Lateral view of the localizations of cortical ECoG electrodes for the entire subject cohort ( $n = 29$ ) plotted in MNI space (MNI152 Nonlinear Asymmetric 2009b (Fonov et al., 2011)). The color of the points represents the average coherence between neural and produced audio data for that electrode. B. Lateral view of the STN with points indicating the location of micro-electrode recordings indicating the coherence index for that electrode with the same color-scale as in A. Note the change of scale as compared to the cortex. C. Locations of macro rings relative to the STN. D. Location of DBS lead contacts relative to the STN. Panels B-D share the same scale.

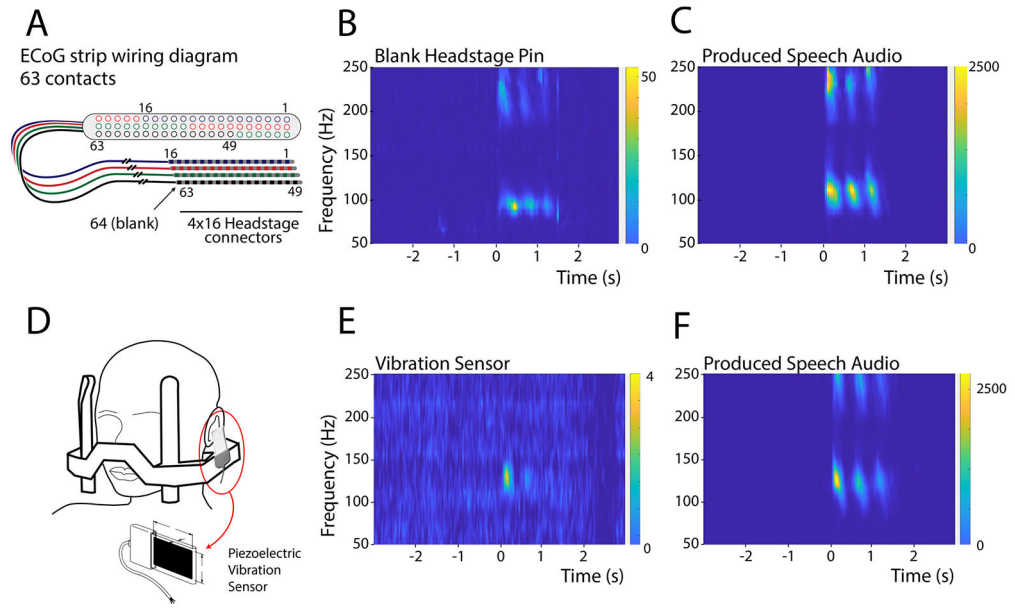


**Fig. 8.** The narrowband component is present in non-neural recordings. A. Schematic of the ECoG electrode strip showing the electrode contact and connector layout. 4 cables of 16 wires are used for the 63 electrodes, resulting in one headstage pin not connected to any electrode on the brain (marked as contact #64). B. Time-frequency plot of the signal recorded from the blank headstage pin (subject DBS3020). C. Spectrogram of the produced speech audio for the same subject as in B. D. A schematic representation of the montage of the vibration sensor on the stereotactic frame. E. Time-frequency plot of the signal recorded from the vibration sensor (subject DBS3029). F. Spectrogram of the produced speech for the same subject as in E. In panels B-C and E-F, zero marks the onset of the speech production.

Percentage ( $\pm$  standard error) of electrodes showing significant similarity between neural data and the produced speech audio or stimulus audio, as established by the coherence method and the Roussel et al.'s (2020) method. The coherence method was run independently for the baseline, listening and speech production epochs. The Roussel et al.'s method used the entire duration of the session. Hierarchical bootstrapping was used to estimate the standard error.

**Table 1**

Audio Method Epoch	Produced speech audio			Stimulus audio				
	Coherence baseline	listening	speech	Roussel all	Coherence baseline	listening	speech	Roussel all
ECoG	0.2 $\pm$ 0.1%	0.2 $\pm$ 0.1%	52 $\pm$ 6%	54 $\pm$ 5%	0.4 $\pm$ 0.3%	0.2 $\pm$ 0.1%	1.4 $\pm$ 0.7%	2.2 $\pm$ 0.5%
Macro	0%	0%	42 $\pm$ 8%	25 $\pm$ 5%	0%	0%	0%	4 $\pm$ 2%
Micro	0%	0%	56 $\pm$ 7%	96 $\pm$ 7%	0%	0%	0%	0.6 $\pm$ 0.8%
DBS Lead	0%	0%	47 $\pm$ 10%	59 $\pm$ 10%	6 $\pm$ 6%	7 $\pm$ 6%	10 $\pm$ 8%	12 $\pm$ 8%
Blank	10 $\pm$ 4%	12 $\pm$ 5%	65 $\pm$ 8%	71 $\pm$ 6%	2 $\pm$ 2%	15 $\pm$ 8	3 $\pm$ 2%	12 $\pm$ 7%

Coherence indices are independent of anatomic location.